

1 **Divergent Sensitivities of Apparent Oxygen Utilization to Circulation** 2 **Ventilation Changes in the Deep Ocean Across Earth System Models**

3 *Damien Couespel^a, Xabier Davila^a, Nadine Goris^a, Emil Jeansson^a, Siv K. Lauvset^a, Jerry Tjiputra^a

4 ^aNORCE Research AS, Bjerknes Centre for Climate Research, Bergen, Norway

5 Corresponding author: daco@norceresearch.no

6 **Abstract**

7 The biological carbon pump (BCP), involving photosynthesis at the surface and remineralisation at depth, maintains a signifi-
8 cant vertical gradient in dissolved inorganic carbon (DIC), thereby promoting the ocean's ability to absorb atmospheric CO₂.
9 Remineralised DIC is a good indicator of the strength of the BCP. It can be estimated from apparent oxygen utilisation (AOU),
10 which measures the deficit of oxygen relative to saturation. AOU is projected to increase under climate change due to changes
11 in remineralisation rates and circulation ventilation. However, the amplitude of the change remains uncertain. Here, we identify
12 linear relationships between trends in AOU and ideal-age in the deep ocean, based on simulations of the contemporary (1982-
13 2013) and future (2015-2099) periods from five Earth system models (ESMs). Our analysis underscores the substantial role of
14 circulation ventilation slowdown in increasing remineralised DIC. Furthermore, the study highlights considerable inter-model
15 variability in their sensitivity of AOU to age changes, with this sensitivity remaining relatively stable over time. With more ob-
16 servational data, refined estimates of age changes from ocean tracers and a larger model ensemble, constraining this variability
17 will become feasible. These insights emphasise both the challenges and opportunities for constraining future BCP projections
18 arising from uncertainties in circulation ventilation.

1 Introduction

The capacity of the ocean to take up and store carbon is driven by the marine carbonate chemistry, the solubility pump and the biological carbon pump (BCP hereafter, accounting for the carbonate and soft-tissue pumps, Volk and Hoffert (1985) and see DeVries (2022) for a review of the ocean carbon cycle). A part of the BCP is the photosynthetic transformation of inorganic carbon to organic carbon at the surface. The organic material is then transported to depth where it is transformed back into its inorganic form through remineralisation. In the deep ocean, remineralised carbon and nutrients are accumulated. This accumulation is an important component of the BCP and is connected to the strength of the ocean overturning circulation, which transports the inorganic carbon and nutrients back to the surface, closing the loop. The BCP is therefore the primary mechanism responsible for keeping the concentration of dissolved inorganic carbon (DIC) low at the surface and high in the interior, resulting in a large vertical gradient of DIC (Volk and Hoffert, 1985; Boyd et al., 2019; DeVries, 2022). This enhances the capacity of the ocean to take up atmospheric CO₂ (Kwon et al., 2009). Without the BCP, atmospheric CO₂ would be more than 200 ppm higher than otherwise (Sarmiento and Toggweiler, 1984; Maier-Reimer et al., 1996; Goodwin et al., 2008; Tjiputra et al., 2025).

Due to competition between the decrease in organic matter export and slower circulation, it is unclear how the role of BCP will change in the future (Frenger et al., 2024). There is a general consensus between state-of-the-art Earth system models (ESMs) that the BCP and the processes involved are impacted by global warming (Wilson et al., 2022), but the amplitude of the change and its response to higher atmospheric CO₂ are both still uncertain. Indicators of the functionality of the BCP are primary production (related to the photosynthetic transformation of carbon at the surface), export production (related to the transport of organic material to depth) and the amount of remineralised carbon. On average, ESMs project a decrease in globally averaged primary production and export production across various future scenarios of increasing atmospheric CO₂ (Henson et al., 2022; Wilson et al., 2022; Kwiatkowski et al., 2020). Yet, these results differ regionally with, e.g., a general increase in the Arctic Ocean, Southern Ocean, and a general decrease in the equatorial Pacific (Myksovoll et al., 2023; Henson et al., 2022; Wilson et al., 2022; Kwiatkowski et al., 2020). Globally and regionally, the range of projected changes in primary production and export production differs largely between ESMs such that the inter-model range of the change is often more than twice its multi-model mean (Tagliabue et al., 2021). In contrast, ~~more remineralisation of organic matter in the~~ greater accumulation of remineralised carbon in the ocean interior can be expected due to a more sluggish circulation (Tjiputra et al., 2018; Weijer et al., 2020), increasing the effectiveness of the BCP despite a reduced export production from the surface (Liu et al., 2023). However, despite model consensus on a global increase of remineralised carbon across scenarios, the amplitude varies widely between models (Wilson et al., 2022).

The quantity of remineralised carbon (DIC_{remin}) is a good indicator of the strength of the BCP and its impact on atmospheric CO₂ (Marinov et al., 2008; Kwon et al., 2009; Koeve et al., 2020; Frenger et al., 2024). In a steady state climate, large DIC_{remin} stocks correspond to low atmospheric CO₂ levels (Marinov et al., 2008; Frenger et al., 2024) and in a transient climate, the strongest increase in DIC_{remin} corresponds to the strongest biologically-induced decline in atmospheric CO₂ (Koeve et al., 2020; Frenger et al., 2024). In contrast, export production is unrelated to atmospheric CO₂ (Marinov et al., 2008; Kwon et al., 2009; Frenger et al., 2024). DIC_{remin} can be estimated from apparent oxygen utilisation (AOU, Frenger et al. (2024); Wilson et al. (2022)), which measures the deficit of oxygen compared to saturation. It is an estimate of the cumulative oxygen utilised to remineralise organic material since the water parcel was last in contact with the atmosphere. Despite some limitations such as assuming 100% oxygen saturation at the surface (Ito et al., 2004), changes in AOU can be used for quantifying the impact of the BCP on atmospheric CO₂ (Koeve et al., 2020).

AOU is traditionally supposed to be the product of the oxygen utilisation rate (OUR) and an estimation of ventilation age, i.e. the time since the water-mass was last in contact with atmosphere (~~Sulpis et al., 2023; Feely et al., 2004; Sarmiento et al., 1990~~ (see for example Sulpis et al. (2023); Guo et al. (2023); Sonnerup et al. (2015); Feely et al. (2004); Sarmiento et al. (1990); Jenkins (1982)). In regions dominated by advection or with an even spatial distribution of the respiration rate, the relation between AOU and ventilation age is linear when both are affected similarly by transport (Koeve and Kähler, 2016). Typically the linear relation-

63 ship breaks in areas where gradients are too different (Thomas et al., 2020). A stronger remineralisation closer to the surface
64 or below highly productive zones (e.g., equatorial Pacific) will locally increase AOU without any correlation to a change in
65 [ventilation](#) age. The linear relation between AOU and [ventilation](#) age has been used to estimate OUR ([Sulpis et al., 2023](#))
66 ([Sulpis et al., 2023](#); [Jenkins, 1982](#)) and as a proxy of water-mass age (Thomas et al., 2020). The relationship between trends or
67 changes in AOU and [ventilation](#) age can further be used to decompose changes in AOU into [circulation-driven](#) [ventilation-driven](#)
68 and biologically-driven factors. So far this relationship has been little explored in future climate projection. Bopp et al. (2017)
69 found a strong relationship in one ESM from the Coupled Model Intercomparison Project Phase 5 (CMIP5), however, ven-
70 tilation ages were not available for the other CMIP5 models. More recently, Liu et al. (2023) explored the relation between
71 changes in circulation and changes in AOU. They found that the slowing down of the meridional overturning circulation, which
72 is an indicator of ocean interior residence time, would allow more time for the exported biogenic carbon to accumulate at depth
73 and thus increase the deep ocean storage of carbon by the BCP.

74 In this work we further explore the relationship between changes in circulation and changes in the BCP using Earth system
75 model simulations from the sixth Coupled Model Intercomparison Project (CMIP6) as well as observations from the Global
76 Ocean Data Analysis Project (GLODAPv2, Lauvset et al. (2024)). Following the approach suggested by Frenger et al. (2024),
77 we use remineralised DIC, estimated from AOU, as indicator for the BCP. We show that changes in AOU are linearly related to
78 changes in [ventilation](#) age in large parts of the deep ocean. We further use the linear relationship to quantify the respective role
79 [circulation-ventilation](#) changes play in the future evolution of the BCP. Lastly, we discuss future opportunities to constrain the
80 estimates of the deep ocean BCP with observations.

81 2 Methods

82 2.1 Earth system models outputs and observational data

83 Eleven Earth system models (ESMs) provide the monthly 3D output fields required to compute AOU for the preindustrial
84 control (piControl), historical and SSP5-8.5 future scenario simulations in a replica of the CMIP6 database. Among these eleven
85 ESMs, only eight also provide outputs for the [age-ideal-age](#) tracer: MPI-ESM1.2-LR and MPI-ESM1.2-HR (Mauritsen et al.,
86 2019), ACCESS-ESM1.5 (Ziehn et al., 2020), IPSL-CM6A-LR (Boucher et al., 2020), MIROC-ES2L (Hajima et al., 2020),
87 NorESM2-LM and NorESM2-MM (Seland et al., 2020) and CanESM5 (Swart et al., 2019). [The ideal-age tracer measures the](#)
88 [time elapsed since a water parcel was last at the ocean surface. It is carried by the simulated ocean circulation and mixing. We](#)
89 [use the ideal-age tracer to estimate the ventilation age of the ESMs.](#) We do not consider NorESM2-MM and MPI-ESM1.2-HR
90 here to keep only one variant of each model. We also do not consider CanESM5 because it does not provide phosphate fields
91 that are used to compute the PO-tracer (Broecker et al., 1991), required to define water-masses (see subsection 2.3). Hence, five
92 ESMs (Table 1) are selected to be analysed in detail in this work. For comparison, we also compute AOU for the four remaining
93 ESMs (CanESM5, CNRM-ESM2-1 (Séférian et al., 2019), GFDL-ESM4 (Dunne et al., 2020), UKESM1-0-LL (Sellar et al.,
94 2020)).

Table 1. The CMIP6 Earth system models analysed in this study, their ocean, sea-ice and marine biogeochemistry, and their ocean grid resolution

ESM	Ocean/sea-ice	Marine biogeochemistry	Ocean grid
ACCESS-ESM1-5 (Ziehn et al., 2020)	MOM5/CICE4	WOMBAT	1°, 50 vertical levels
IPSL-CM6A-LR (Boucher et al., 2020)	NEMOv3.6/LIM3	PISCESv2	1°, 75 vertical levels
MIROC-ES2L (Hajima et al., 2020)	COCO	OECO2	1°, 62 vertical levels
MPI-ESM1-2-LR (Mauritsen et al., 2019)	MPIOM1.6	HAMOCC6	1.5°, 40 vertical levels
NorESM2-LM (Seland et al., 2020)	BLOM/CICE5	iHAMOCC	1°, 70 vertical levels

95 To have an observational baseline over the recent period, we also conduct an observation-based analysis of the trends in AOU
96 and trends in [ventilation](#) age using the observational data product GLODAPv2 (2016) (Key et al., 2015; Olsen et al., 2016). We

97 use temperature, salinity, phosphate and oxygen measurements. AOU is computed in the same way as for the ESMs (subsection
 98 2.2). We use the [ventilation](#) age product from Jeansson et al. (2021). In this product, measurements of the chlorofluorocarbon
 99 CFC-12 from GLODAPv2 (2016) are used with the transit time distribution (TTD) method to compute [ventilation](#) age, assuming
 100 100 % saturation and a balance between advection and mixing, i.e. $\Delta/\Gamma = 1$. We only use data points where measurements
 101 of all variables mentioned are available. In order to be consistent with the [ventilation](#) age product, we opted for GLODAPv2
 102 (2016), although more recent versions of the observational data product are available (e.g. Lauvset et al. (2024)). The time
 103 range of the observational baseline is limited by the [ventilation](#) age dataset and extends from 1982 to 2013. Only observations
 104 below 1000 metres are considered to avoid the influence of mixed-layer processes and subtropical gyres.

105 2.2 Apparent oxygen utilisation and remineralised carbon

106 Apparent oxygen utilisation (AOU in $[\text{mol O}_2 \text{ m}^{-3}]$) is computed as:

$$107 \quad \text{AOU} = O_2^{\text{sat}} - O_2 \quad \text{Equation 1.}$$

108 where O_2 is the in-situ dissolved oxygen concentration and O_2^{sat} is the dissolved oxygen concentration at saturation computed
 109 from temperature and salinity following Garcia and Gordon (1993, 1992). The amount of carbon resulting from this remineral-
 110 isation ($\text{DIC}_{\text{remin}}$ in $[\text{g C m}^{-3}]$) is estimated as:

$$111 \quad \text{DIC}_{\text{remin}} = m_{\text{C}} \times R_{\text{C:O}_2} \times \text{AOU} \quad \text{Equation 2.}$$

112 where m_{C} is the molecular weight of carbon (12.01 g mol^{-1}) and $R_{\text{C:O}_2}$ is the stoichiometric ratio between carbon and oxygen
 113 (117:170, Anderson and Sarmiento (1994)).

114 Although providing a reasonably good indication of the BCP strength and its impact on atmospheric CO_2 (Koeve et al., 2020;
 115 Frenger et al., 2024), AOU has a couple of pitfalls that should be kept in mind. First, it assumes that at the surface, oxygen
 116 concentration is in equilibrium with the atmosphere. This assumption is valid in most of the ocean, yet in high latitudes, water
 117 parcels can be detrained from the mixed layer while being under-saturated leading to an overestimation of respiration and
 118 AOU, notably in the deep ocean (Ito et al., 2004; Duteil et al., 2013). True Oxygen utilisation (Ito et al., 2004) or Evaluated
 119 Oxygen utilisation (Duteil et al., 2013) are intended to overcome this limitation. However, the computation of these variables
 120 requires additional tracers (e.g., preformed O_2 , (Tjiputra et al., 2020)) that are not routinely available in the CMIP6 output
 121 database. Another limitation is that AOU only measures aerobic remineralisation. Yet, when oxygen levels are too low,
 122 anaerobic remineralisation will take place and use other oxidants (e.g., nitrate for denitrification) instead of oxygen. In the open
 123 ocean, denitrification typically occurs in suboxic waters, when oxygen concentrations drop below $5 \mu\text{mol O}_2 \text{ l}^{-1}$ (Keeling et al.,
 124 2010). Suboxic waters represent only 0.1% of the contemporary ocean and are located in the upper 1000 metres (Deutsch et al.,
 125 2011; Keeling et al., 2010). During the 21st century, suboxic volume may extend but is projected to not exceed 1% of the ocean
 126 volume (Deutsch et al., 2011; Cocco et al., 2013; Fu et al., 2018).

127 2.3 Definition of water-masses

128 We aim to find a linear relationship between the spatial distribution of AOU trends and [ventilation](#) age trends that is representa-
 129 tive for most of the deep ocean. From now on and unless specified otherwise, we define the deep ocean as the ocean below 1000
 130 metres. We assess the linear relationship within different water-masses of the deep ocean characterized with a combination of
 131 the PO-tracer (PO^* , Broecker et al. (1991)) and density.

132 For the water-mass definition of the ESMs, neither density nor PO^* are standard outputs in the CMIP6 database so that
 133 we compute density with the Gibbs SeaWater (GSW) Oceanographic Toolbox of TEOS-10 in xarray (Caneill and Barna,
 134 2024; McDougall and Barker, 2011) and PO^* based on the definition by Broecker et al. (1991) ($\text{PO}^* = \text{PO}_4 + O_2/175 -$
 135 $1.95 \mu\text{mol PO}_4 \text{ kg}^{-1}$). Both variables are averaged over the years 1982 to 2013, i.e., the time period covered by the observational

dataset used in this work. Our water-mass definition for the ESMs focuses only on the deep ocean and uses PO^* -thresholds to define water-masses originating in the North Atlantic and Southern Ocean. Broecker et al. (1998) state that the global distribution of PO^* has its minimum in the North Atlantic, its maximum in Southern Ocean and that the PO^* distribution for deep waters formed in the North Atlantic is very distinct from the distribution for deep waters formed in the Southern Ocean. Based on these statements, we defined the PO^* -thresholds for deep ocean ~~water-masses~~water-masses individually for each ESM, using PO^* averaged on 1982-2013 and applying the following approach: (i) We compute the 95th percentile of the PO^* distribution in the deep subpolar North Atlantic, between 40-60°N and 0-70°E. (ii) We compute the 5th percentile of the PO^* distribution in the deep Southern Ocean, south of 55°S. (iii) The PO^* -threshold is defined as the average between the aforementioned percentiles. We find that Atlantic water-masses have PO^* values below the threshold while Southern water-masses have PO^* values above the threshold (see supplementary Fig. S1). For the Southern water-masses, it is necessary to exclude grid-cells located north of 60°N as some Arctic Ocean grid-cells would otherwise be included without being continuously connected to the Southern Ocean. All longitudes are considered for the Southern water-masses. For the Atlantic water-masses, only grid-cells located east of the Drake passage, west of 30°E and south of 80°N are included to exclude grid-cells in the Pacific and Indian Oceans that fulfil the PO^* -threshold and to exclude grid-cells in the Arctic Ocean. In the Arctic Ocean, a linear relationship between AOU trends and ventilation age trends emerges but with a very different slope than the one found for the Atlantic water-masses: here, AOU trends seem to be much more sensitive to ventilation age trends (not shown). Since our focus is on identifying linear relationships representative for most of the deep global ocean, we decided to exclude the Arctic from the analysis. We split the Southern and Northern ~~water-masses~~water-masses into half according to density (supplementary Table S1), leading to four water-masses: (i) the Atlantic light waters, (ii) the Atlantic dense waters, (iii) the Southern light waters, and (iv) the Southern dense waters. These four water-masses cover at least 70 % of the entire deep ocean, depending on the ESM (70 % for IPSL-CM6A-LR and at least 92 % for the other models). For each water-mass and each ESM we define a spatial mask (supplementary Fig. S2), which is used to identify grid points belonging to the same water-mass and compute the linear regression between trends in AOU and trends in ventilation age (subsection 2.4). We keep the masks constant throughout the historical and SSP5-8.5 simulations as the masks show minimal sensitivity to the time period used for creating the PO^* and density fields (supplementary Figs. S2 and S3).

Similar to the definition of water-masses used for the ESMs, observational data points are classified into water-masses originating from the Southern Ocean and North Atlantic (supplementary Fig. S4) based on their PO^* values. Waters originating in the Southern Ocean are defined via $1.2 \leq PO^* \leq 2.0 \mu\text{molPO}_4 \text{kg}^{-1}$ and those originating in the North Atlantic Ocean via $PO^* < 1.2 \mu\text{molPO}_4 \text{kg}^{-1}$ with PO^* -thresholds based on Broecker et al. (1998). ~~In lighter density classes, due to the fanning out of temperature and salinity, the number of data is too low to identify a relationship between AOU trends and age trends.~~ Most of the data points used in this work belong to the densest half of waters originating from the North Atlantic Ocean or the Southern Ocean (98 % and 75 % of the points respectively). They were therefore not further separated into light and dense waters. The water-masses will be referred to as Southern dense waters and North Atlantic dense waters to facilitate a meaningful comparison with their model counterparts and are most representative of the water-mass end members.

2.4 Relationship between trends in AOU and trends in ventilation age

Just as the relationship between AOU and ventilation age can be linear (Sulpis et al., 2023), one might expect that the trends in AOU and the trends in ventilation age can be linearly related. In this work we intend to express the trends in AOU ($\frac{d\text{AOU}}{dt}$) via trends in ventilation age ($\frac{d\text{age}}{dt}$), in each point X, as follows:

$$\frac{d\text{AOU}}{dt}(X) = S_{\Delta\text{age}}^{\Delta\text{AOU}} \times \frac{d\text{age}}{dt}(X) + B + \varepsilon(X). \quad \text{Equation 3.}$$

We assess the linear relationship between spatial fields of AOU trends and ventilation age trends within the previously define water-masses using a linear regression (Virtanen et al., 2020). The slope of the linear regression is the sensitivity of AOU changes to ventilation age changes ($S_{\Delta\text{age}}^{\Delta\text{AOU}}$). The intercept of the linear regression, B , represents a spatial average of the changes in AOU when there is no change in ventilation age. $\varepsilon(X)$ is the error of the linear regression in each point.

179 All together, $B + \varepsilon$ represents the change in AOU that is not linearly related to changes in [ventilation](#) age, e.g. changes
 180 in remineralisation rates. $S_{\Delta\text{age}}^{\Delta\text{AOU}}$ defined here is connected to the oxygen utilisation rate (OUR) defined in other studies
 181 ([Sulpis et al., 2023](#); [Feely et al., 2004](#)). (e.g. [Sulpis et al. \(2023\)](#); [Guo et al. \(2023\)](#); [Sonnerup et al. \(2015\)](#); [Feely et al. \(2004\)](#); [Sarmiento et al.](#)
 182). Indeed, if the equation $\text{AOU} = \text{OUR} \times \text{age}$ is differentiated with respect to time, then $S_{\Delta\text{age}}^{\Delta\text{AOU}}$ and OUR are a similar quantity:
 183 an estimate of a spatio-temporal average of the local instantaneous oxygen utilisation rate. We choose to call the slope of the lin-
 184 ear regression $S_{\Delta\text{age}}^{\Delta\text{AOU}}$ instead of OUR for two reasons: 1) we think this word conveys more accurately the purpose of the analysis,
 185 i.e. [investigating our investigation of](#) the relationship between AOU trends and [ventilation](#) age trends and 2) we want to avoid
 186 ambiguity with studies [working at estimating OUR](#) (e.g. [Sulpis et al. \(2023\)](#); [Guo et al. \(2023\)](#); [Jenkins \(1982\)](#)) [estimating](#)
 187 [OUR using AOU and ventilation age](#) (e.g. [Sulpis et al. \(2023\)](#); [Guo et al. \(2023\)](#); [Sonnerup et al. \(2015\)](#); [Feely et al. \(2004\)](#); [Sarmiento et al.](#)
 188) [and not their temporal trends](#).

189 For the analysis of the ESMs, it is crucial to estimate and remove the drift in the simulated fields of AOU and [ventilation](#)
 190 age tracer before calculating their respective trends. The drifts are estimated for every ocean grid-cell of the ESMs using
 191 a linear regression over 250 years of the piControl simulation, starting from the year in the piControl simulation where the
 192 historical simulation has been initialised (supplementary Table S2). Outputs from the historical and SSP5-8.5 simulations are
 193 then drift corrected for each point in time t ($X_{\text{drift-corrected}}(t) = X_{\text{drift-uncorrected}}(t) - (t - t_0) \times \text{drift}$, with t_0 referring to 1850)
 194 before computing the trends. The trends are computed using a linear regression over the years (i) 1982-2013 of the historical
 195 simulation to match the time period of available observational data and (ii) 2015-2099 (the entire SSP5-8.5 simulation). When
 196 considering the ESMs, for the time period 1982-2013, between 49 % (NorESM2-LM) and 72 % (IPSL-CM6A-LR, MIROC-
 197 ES2L) of the deep ocean grid points have significant trends (p-value ≤ 0.05) in both AOU and [ventilation](#) age, while between
 198 84 % (NorESM2-LM) and 94 % (MIROC-ES2L) have significant trends for the time-period 2015-2099 (supplementary Fig.
 199 S5). The non-significant trends are very close to zero. For each ESM, we only consider grid-points with significant trends for
 200 computing the linear regression in each water-mass.

201 To overcome the difficulty of identifying trends with highly spatio-temporally sparse observational data, as it is the case for
 202 [ventilation](#) age estimates, we collapse the available observations in temperature-salinity (T-S) space. Trends in AOU and
 203 [ventilation](#) age are computed within bins in the T-S space (supplementary Fig. S6). To ensure that data points are geographically
 204 close to each other within each T-S bin, we (i) remove outliers defined as data points geographically further than twice the
 205 median distance to the median location and (ii) only keep points that are within a maximum distance from the median location
 206 (recomputed without the outliers). Thus the computation of the trends depends on two choices: the temperature and salinity
 207 resolution for the T-S bins and the maximum distance from the median location within each T-S bins. These choices affect:
 208 (i) the grouping of comparable measurements into the same T-S bin, regardless of their geographical location, (ii) the number
 209 of data points per T-S bin needed to identify significant trends (p-value ≤ 0.05), and (iii) the number of trend estimates (one
 210 per T-S bin) required to establish a significant (p-value ≤ 0.05) correlation between AOU trends and [ventilation](#) age trends.
 211 Trends for AOU and [ventilation](#) age, ($d\text{AOU}/dt$) and ($d\text{age}/dt$) are computed when five or more observations are grouped into
 212 a given T-S bin. Due to the substantial influence of the T-S bin size and the maximum distance, we conduct the analysis of the
 213 observational data 625 times with different random choices of these parameters to derive a distribution of the observation-based
 214 $S_{\Delta\text{age}}^{\Delta\text{AOU}}$. Temperature/salinity resolutions ranged from 0.026°C to 0.325°C and 0.0024 to 0.03 , while maximum distance from
 215 500 km to 5000 km . Trends are then grouped into the Southern and Atlantic water-masses defined previously. Finally, as in the
 216 modelling counterpart of the analysis, a linear regression is computed between the spatial distributions of AOU trends and the
 217 [ventilation](#) age trends.

218 In this work we apply linear regressions for estimating trends and evaluating linear relationships. Further, we evaluate the
 219 significance of the trends and the linear relationship base on the p-values testing the null hypothesis of zero slopes, i.e. no
 220 trends or no linear relationship. When the p-value is lower than or equal to 0.05 we consider the trends or the linear relationship
 221 to be significant. The linear regression also provides a 95 % confidence interval for the slope, serving as a measure of the
 222 uncertainty associated with $S_{\Delta\text{age}}^{\Delta\text{AOU}}$. If this uncertainty is not specifically stated, it means that it is negligible with respect to the
 223 number of significant figures provided.

2.5 Evaluation of model-observation comparability

The analytical approach applied to observational data differs from the one applied to model outputs in three ways. (1) For the observational data, ventilation age is estimated using the TTD method with measurements of CFC-12. This method compares measured CFC-12 concentrations in the ocean with the evolution of CFC-12 concentrations in the atmosphere, assuming some balance between mixing and advection in ocean circulation. ~~However, ESMs calculate the~~ ESMs estimate the ventilation age via the ~~tracer-ideal-age~~, which is carried by the simulated ocean circulation and ageing at a rate of one year per year once it has left the tracer, which counts the elapsed time since the last contact with the ocean surface. Hereafter, where necessary, we will distinguish between "ideal-age" and "TTD-mean-age", the latter referring to age estimates derived from CFC-12. Where no distinction between the two is necessary, we will simply refer to "ventilation age". (2) Observational datasets suffer from sparse and heterogeneous sampling in space and time, whereas ESM model results cover the entire ocean on a regular grid with monthly frequency. (3) Because the number of observational data is limited, trends must be computed within T-S bins while the outputs from ESMs gives time series for each grid-point.

We quantify the uncertainties in $S_{\Delta\text{age}}^{\Delta\text{AOU}}$ estimates derived from the observational dataset related to the aforementioned limitations using outputs from the NorESM2-LM historical simulation. We run two analysis:

- In TTD-UNC we quantify the uncertainties related to using the TTD method. To do so, we applied the TTD method to CFC-12 outputs from NorESM2-LM. Then, similar to the analysis of the ESMs ensemble (section 2.4), (i) we compute trends in TTD-mean-age, (ii) we identify a linear relationship between the spatial fields of AOU trends and TTD-mean-age trends in the Atlantic dense and Southern dense water-masses and (iii) we derive $S_{\Delta\text{age}}^{\Delta\text{AOU}}$ values. In NorESM2-LM simulations, CFC-12 only partially invaded the ocean; e.g. most of the Pacific and Indian Oceans north of 40°S have CFC-12 concentration too small to derive a TTD-mean-age. Thus, in this analysis, we also sample the ideal-age outputs based on the spatio-temporal distribution of TTD-mean-age and derive reference values of $S_{\Delta\text{age}}^{\Delta\text{AOU}}$ using this ideal-age sample for the Atlantic dense and Southern dense water-masses. $S_{\Delta\text{age}}^{\Delta\text{AOU}}$ values derived from TTD-mean-age is compared against the reference $S_{\Delta\text{age}}^{\Delta\text{AOU}}$ values derived from ideal-age to quantify the uncertainty due to the TTD method.
- In SAMPLE-UNC, we quantify uncertainties due to data scarcity and the necessity to compute trends in T-S bins. We sample in space and time the NorESM2-LM outputs based on the observational data and replicate the analysis applied to the observational datasets, i.e. trends computed in T-S bins with the same 625 choices for T-S bins sizes and maximum distance that were used for the analysis of the observational dataset. The comparison between the obtained distribution of $S_{\Delta\text{age}}^{\Delta\text{AOU}}$ and the original $S_{\Delta\text{age}}^{\Delta\text{AOU}}$ values (no sampling, trends computed in each grid-point) quantifies the uncertainty of the T-S bins approach as well as of the data scarcity.

3 Results

3.1 Contemporary and future AOU across Earth system models

Contemporary spatial AOU patterns reflect physical transport and biological oxygen consumption. For example, AOU is particularly high in areas combining weak ventilation or ventilation of oxygen-depleted water-masses and intense remineralisation such as the deep ocean, the North Pacific or in the upper 1000 metres in the equatorial band (Fig. 1a,b,c). Earth system models (ESMs) reproduce the general patterns shown by gap-filled observational products from the World Ocean Atlas 2023 (supplementary Fig. S7), yet with some regional strong positive and negative biases relative to observations (Fig. 1d,e,f). On average, ESMs overestimate AOU in the ocean deeper than 2000 metres north of ca. 40°S and below 1000 metres in the Pacific north of ca. 50°S. In contrast, ESMs underestimate AOU in the Southern Ocean (south of ca. 30°S) and above 1000 metres in the northern hemisphere. In addition to biases in the model-mean, we note that there is a strong inter-model spread in large parts of the ocean, where the range of ESM values is higher than 70 % of the observation value (stippling in Fig. 1d,e,f and

264 supplementary Fig. S8).

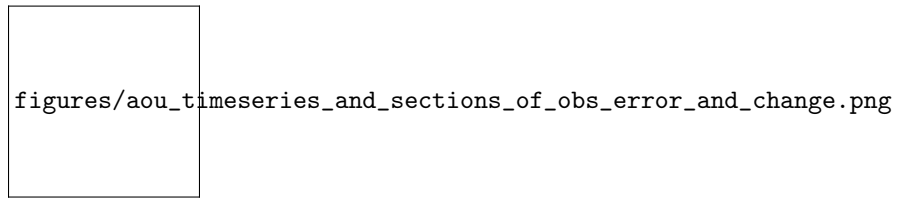


Figure 1. Evaluation of the simulated AOU and consistency in the projected change (Δ AOU). (a, b, c) AOU from the World Ocean Atlas 2023 (WOA23, Garcia et al. (2024)), averaged over 1971-2000 in the Atlantic (10°W to 60°W), Pacific (130°W to 180°W) and Indian (40°E to 90°E) sectors. (d, e, f) Multi-model mean of AOU bias against WOA23. Stippling shows AOU uncertainty in ESMs, i.e. when the range between the highest and lowest ESM values is greater than 70 % of the WOA23 value. Refer to supplementary Fig. S8 for individual ESM bias. (g, h, i) Multi-model mean of projected change (1971-2000 minus 2070-2099) under the SSP5-8.5 scenario, zonally average. Stippling shows Δ AOU uncertainty in ESMs, i.e. when the range between the strongest and weakest Δ AOU exceed three times the multi-model mean Δ AOU. Refer to supplementary Fig. S9 for individual ESM Δ AOU. The red dashed lines indicate the 1000 metres separating the upper and deep ocean. (j, k, l) Time series of Δ AOU integrated on the (j) global, (k) upper and (l) deep ocean for each ESM considered in this study. The gray shading shows the range of other ESMs not used in this study (CanESM5, CNRM-ESM2-1, GFDL-ESM4, UKESM1-0-LL). The vertical dashed gray line (year 2015) separates the historical and SSP5-8.5 scenarios.

265 In the majority of the ocean, AOU is projected to increase under the SSP5-8.5 scenario (Fig. 1g,h,i). Most of the increase
266 occurs below 1000 metres (Fig. 1l), with agreement on the sign of change among the models (supplementary Fig. S9). Above
267 1000 metres, AOU is projected to decrease in areas around the Equator or near the surface in the high latitude (Fig. 1g,h,i).
268 The uncertainty of the projected change is considerable between ESMs with the inter-model spread exceeding three times the
269 multi-model mean in the intermediate depth of the Pacific, in the low-latitude Indian, and in the deep subtropical North Atlantic
270 (stippling in Fig. 1g,h,i and supplementary Fig. S9). By 2099, the integrated projected global change in AOU compared to 1850
271 ranges from 20 to 76 PgC (Fig. 1j). A substantial share of the inter-model uncertainty in AOU changes stems from the deep
272 ocean (below 1000 metres). Here, the ESM spread encompasses 20 to 65 PgC (Fig. 1l), while it ranges from -10 to 25 PgC
273 above 1000 metres (Fig. 1k). The inter-model differences in AOU changes within the ESMs used in this study is representative
274 of the inter-model differences in the AOU changes as seen by other ESMs (grey shading in Fig. 1j,k,l).

275 3.2 $S_{\Delta \text{age}}^{\Delta \text{AOU}}$ across Earth system models

276 For our model ensemble and the grid-points with significant trends in AOU and ideal-age in our defined Atlantic and South-
277 ern water-masses, the AOU trends are significantly correlated with the ideal-age trends for the years 1982-2013 (Fig. 2 and
278 supplementary Fig. S10) and 2015-2099 (supplementary Fig. S11). [When ideal-age increases or decreases due to changes in
279 ventilation rates or redistribution of waters, AOU increases or decreases, respectively.](#) In at least four out of five ESMs, spatial
280 variability in ideal-age trends can explain more than half of the spatial variability in AOU trends in all four water-masses for
281 the contemporary period, i.e. the coefficient of determination R^2 is higher than 0.5. Weaker correlations are potentially related
282 to significant contribution of mixing over advection, spatial variability or local changes of respiration rate, or a partially inap-
283 propriate definition of water-masses. For example, in MPI-ESM1.2-LR, some of the grid-points included in the Atlantic light
284 waters could be included in the Atlantic dense waters. Indeed, these grid points have densities very close to the median, their
285 depths are comparable to those of Atlantic dense waters and they exhibit a linear relationship more similar to the one in Atlantic
286 dense waters. For IPSL-CM6A-LR, in some grid-points of the Atlantic dense waters ideal-age unexpectedly increases while
287 AOU decreases. These grid points, located in the Nordic Seas at approximately 3000 meters depth, may have a different history
288 compared to other Atlantic waters and thus would require a separate definition for their [water-mass](#). In most ESMs,
289 the correlation between AOU and ideal-age trends is weaker in the future period for all water-masses except the Southern dense
290 waters, as indicated by the red vertical dashes in Fig. 3 (refer also to supplementary Fig. S14). Hence, ideal-age contributes
291 less to the spatial variability of AOU. Depending on the ESM, our analysis covers only between 43 % and 66 % of the deep
292 ocean for the 1982-2013 period, because i) we only consider grid points with significant trends in ideal-age and AOU, and ii)
293 large part of the deep ocean have weak and non-significant trends during the contemporary period. For the 2015-2099 period,
294 the linear regression analysis covers between 65 % and 94 % of the deep ocean, as the trends are stronger and more significant

295 (supplementary Figs. S11 and S5). The inclusion of the non-significant trends decreases R^2 but does not substantially alter the
296 slope of the linear regression (supplementary Figs. S12 and S13).

260307_REVISION2/figures/scatter_plot_aou_trend_vs_age_trend_historical_1982-2013_signif.png

Figure 2. Distribution of the trends in ideal-age and trends in apparent oxygen utilisation (AOU) for the contemporary period (1982-2013) simulated with five Earth system models (ESMs): a) MPI-ESM1.2-LR, b) ACCESS-ESM1.5, c) IPSL-CM6A-LR, d) MIROC-ES2L, e) NorESM2-LM. The blue shading shows the number of data point for each bin of ideal-age trends and AOU trends for the Southern and Atlantic light/dense waters, accounting only for grid-points where ideal-age and AOU trends are significant. A linear regression is computed between the AOU trends and ideal-age trends for each water-mass. On each panel, the slope ($S_{\Delta\text{age}}^{\Delta\text{AOU}}$), the coefficient of determination (R^2) and the fraction of the deep ocean volume are shown in different colours for each water-mass. The gray shading show the distribution of trends for the entire ocean.

297 The simulated sensitivities of AOU change to ideal-age change ($S_{\Delta\text{age}}^{\Delta\text{AOU}}$) are relatively similar for both light and dense waters.
298 Yet, $S_{\Delta\text{age}}^{\Delta\text{AOU}}$ is slightly stronger in light waters, likely due to stronger remineralisation in the shallower regions. Within each
299 water-mass, $S_{\Delta\text{age}}^{\Delta\text{AOU}}$ varies substantially, increasing by at least a factor of two between the least and the most sensitive ESM. We
300 find that ESMs with a large (small) $S_{\Delta\text{age}}^{\Delta\text{AOU}}$ in the contemporary period (1982-2013) also have a large (small) $S_{\Delta\text{age}}^{\Delta\text{AOU}}$ for the future
301 period under the high CO₂ future scenario SSP5-8.5 (Fig. 3). The linear relation between present and future $S_{\Delta\text{age}}^{\Delta\text{AOU}}$ is strong for
302 the Southern waters across our model ensemble, as indicated by the linear regression giving coefficients of determination higher
303 than 0.97 and p-values below 0.01 (Fig. 3). In the Atlantic waters, the linear relationship is not significant (p-value > 0.05),
304 mostly due to the distinct behaviour of two models. Specifically, $S_{\Delta\text{age}}^{\Delta\text{AOU}}$ in NorESM2-LM does not decline in the future period
305 for Atlantic light waters, and $S_{\Delta\text{age}}^{\Delta\text{AOU}}$ in MIROC-ES2L shows a substantial decrease in the future period for Atlantic dense
306 waters.

figures/constraint_plot_linreg Δ AOUvs Δ Age_in_SSP585_vs_linreg Δ

Figure 3. Distribution of the sensitivity of AOU change to ideal-age change ($S_{\Delta\text{Age}}^{\Delta\text{AOU}}$) in each water-mass: a) Southern light, b) Atlantic light, c) Southern dense, and d) Atlantic dense. Each dot shows the $S_{\Delta\text{Age}}^{\Delta\text{AOU}}$ for one Earth system model (ESM) on the contemporary (1982-2013) and future (2015-2099) period. For few models, the red horizontal/vertical dash indicates a weak correlation ($R^2 < 0.5$) between AOU trends and ideal-age trends for the contemporary/future period. The black line shows the linear regression and the gray shading its confidence interval. The associated coefficient of determination (R^2) and the p-value are indicated in each panel. The diagonal dashed gray line is the 1:1 line.

307 Once a linear relationship has been established providing the average trend in AOU for a given trend in ideal-age, we can use
308 it to further quantify the contribution of ideal-age trends to the trends in AOU in each ESM. This contribution is estimated by
309 multiplying the ideal-age trends with $S_{\Delta\text{Age}}^{\Delta\text{AOU}}$ for each of the four water-masses ($S_{\Delta\text{Age}}^{\Delta\text{AOU}} \times \frac{\text{dage}}{\text{dt}}$ in Eq. 3). Globally integrated,
310 ideal-age trends contribute between 43 % (ACCESSM-ESM1.5) and 106 % (IPSL-CM6A-LR) to the AOU trends in these water-
311 masses (Fig. 4). The disparities in the contributions of ideal-age trends across models arise from differences in the both
312 the ideal-age trends themselves and in $S_{\Delta\text{Age}}^{\Delta\text{AOU}}$. MPI-ESM1.2-LR and ACCESS-ESM1.5 are the two models with the lowest
313 contributions of ideal-age trends but for different reasons: MPI-ESM1.2-LR has the lowest $S_{\Delta\text{Age}}^{\Delta\text{AOU}}$ and relatively strong ideal-age
314 trends, while ACCESS-ESM1.5 has high $S_{\Delta\text{Age}}^{\Delta\text{AOU}}$ and weak ideal-age trends. In contrast to these two models with compensating
315 $S_{\Delta\text{Age}}^{\Delta\text{AOU}}$ and ideal-age trends, MIROC-ES2L shows both a high $S_{\Delta\text{Age}}^{\Delta\text{AOU}}$ and strong ideal-age trends. This combination leads to
316 MIROC-ESL having the highest contribution of ideal-age trends to AOU trends.

317 In general, the positive trends in AOU mostly arise from the Southern dense water-mass, and are driven by positive trends in
318 ideal-age (Fig. 5). The Atlantic dense water-mass exhibits also intense local positive AOU trends driven by ideal-age trends.
319 In these two ventilation regions, the models suggest a weakening in the ventilation rates in the future (increasing ideal-age).
320 In contrast, negative AOU trends are mostly located in the Southern and Atlantic light water-masses, found between 1000 and
321 2000 metres in the subtropics and equatorial region. In these areas, negative ideal-age trends play a major role indicating that
322 waters get younger because of a shift in water-mass structure or stronger ventilation, though stronger ventilation seems less
323 likely considering that stratification increase everywhere in the ocean in the future simulation (Kwiatkowski et al., 2020). Such
324 distinction between light and dense water-masses have been previously identified for the contemporary period in the Nordic
325 Seas (Jeansson et al., 2023). The remainder term, $B + \varepsilon$, locally either slightly compensates or reinforces changes driven by
326 ideal-age trends, resulting globally in a positive contribution to AOU trends.

327 3.3 $S_{\Delta\text{Age}}^{\Delta\text{AOU}}$ from observational data

328 A positive linear correlation is also found between the significant trends in AOU and TTD-mean-age from the observa-
329 tion dataset (supplementary Fig. S15). $S_{\Delta\text{Age}}^{\Delta\text{AOU}}$ evaluated from the observational dataset are 0.04 ± 0.04 and 0.05 ± 0.01
330 $\text{mmol O}_2 \text{ m}^{-3} \text{ yr}^{-1}$ for the Southern dense and Atlantic dense water-masses, respectively (supplementary Fig. S15). Here,
331 the water-masses have not been split into light and dense waters due to the limited number of data points (see subsection 2.3).
332 For both water-masses, the coefficient of determination, R^2 , varies between 0.2 and 1 depending on the methodological choices
333 for the analysis, with higher R^2 values typically associated with higher $S_{\Delta\text{Age}}^{\Delta\text{AOU}}$.

334 The scarcity of observational data and the use of the TTD-mean-age introduce uncertainties into the observation-based $S_{\Delta\text{Age}}^{\Delta\text{AOU}}$.
335 When the analysis is replicated with a sample of NorESM2-LM outputs (SAMPLE-UNC analysis, see subsection 2.5), $S_{\Delta\text{Age}}^{\Delta\text{AOU}}$
336 estimates are 0.17 ± 0.04 and 0.18 ± 0.04 $\text{mmol O}_2 \text{ m}^{-3} \text{ yr}^{-1}$, for the Southern dense and Atlantic dense water-masses, respec-
337 tively (Table 2). This is an increase of 0.08 and 0.04 $\text{mmol O}_2 \text{ m}^{-3} \text{ yr}^{-1}$ when compared to the reference values (analysis with
338 non-scarce data). Using trends in TTD-mean-age as an estimate of trends in ventilation age introduce further uncertainties in
339 the estimate of $S_{\Delta\text{Age}}^{\Delta\text{AOU}}$ from the observational dataset (TTD-UNC analysis, see subsection 2.5). When computed with CFC-12

260307_REVISION2/figures/barplot_AOUtrend_OURxAgetrend_reminder_global_integral.png

Figure 4. Spatially integrated trend in apparent oxygen utilisation ($\frac{d\text{AOU}}{dt}$, dark and light grey) and the contribution from trends in ideal-age ($S_{\Delta\text{age}}^{\text{AAOU}} \times \frac{d\text{age}}{dt}$) under the SSP5-8.5 climate change scenario simulated with five Earth system models (ESMs): MPI-ESM1.2-LR, ACCESS-ESM1.5, IPSL-CM6A-LR, MIROC-ES2L, NorESM2-LM. The remainder ($B + \epsilon$, pink) is computed as the difference between the two aforementioned components (see Eq. 3). Shown are the trends integrated over the global ocean (light grey), and over the water-masses considered in this study. Trends are computed for the period from 2015 to 2099.

Table 2. Sensitivity of AOU trends to [ventilation](#) age trends ($S_{\Delta\text{age}}^{\text{AAOU}}$ in $\text{mmol O}_2 \text{ m}^{-3} \text{ yr}^{-1}$) estimated from the observational dataset and the uncertainty analyses using NorESM2-LM outputs (SAMPLE-UNC and TTD-UNC). For the analysis of the observational dataset and SAMPLE-UNC, values are the mean \pm one standard deviation of the $S_{\Delta\text{age}}^{\text{AAOU}}$ distribution derived from the 625 analyses performed. The reference values in bracket are: for the SAMPLE-UNC analysis, $S_{\Delta\text{age}}^{\text{AAOU}}$ computed with non-scarce data and, for the TTD-UNC analysis, $S_{\Delta\text{age}}^{\text{AAOU}}$ derived using trends in ideal-age.

Analysis	Southern dense	Atlantic dense
Obs. dataset	0.04 ± 0.04	0.05 ± 0.01
SAMPLE-UNC	0.17 ± 0.04 (ref: 0.09)	0.18 ± 0.04 (ref: 0.14)
TTD-UNC	0.01 (ref: 0.10)	0.05 (ref: 0.13)

340 outputs from NorESM2-LM, trends in TTD-mean-age are generally much stronger than trends in ideal-age (not shown). In
 341 some instances, trends may even oppose each other. In consequence, $S_{\Delta\text{age}}^{\text{AAOU}}$ derived from TTD-mean-age is 0.01 and 0.05
 342 $\text{mmol O}_2 \text{ m}^{-3} \text{ yr}^{-1}$ for the Southern dense and Atlantic dense water-masses, respectively (Table 2). This is 0.09 and 0.08
 343 $\text{mmol O}_2 \text{ m}^{-3} \text{ yr}^{-1}$ lower than the reference values ($S_{\Delta\text{age}}^{\text{AAOU}}$ derived from ideal-age). Hence, using trends in TTD-mean-age
 344 lead to underestimation of observation-based $S_{\Delta\text{age}}^{\text{AAOU}}$ while the scarcity of data points and the need to compute trends in the
 345 T-S space results in overestimating it. Together, these overestimation and underestimation compromise the comparability of
 346 observation-based $S_{\Delta\text{age}}^{\text{AAOU}}$ with $S_{\Delta\text{age}}^{\text{AAOU}}$ derived from the ESMs.

347 4 Discussion

348 Our results highlight the importance of [circulation-ventilation](#) changes on the changes in AOU and therefore on $\text{DIC}_{\text{remin}}$ in the
 349 deep ocean. Previous studies suggested that circulation was the main driver of changes in interior carbon content during the
 350 past and future climate (Bopp et al., 2017; Kessler et al., 2018; Liu and Primeau, 2023). We quantify that between 2015 and
 351 2099, under the SSP5-8.5 climate change scenario and in the ocean below 1000 metres, a [circulation-ventilation](#) slow down
 352 contributes between 43 % and 106 % to the increase in $\text{DIC}_{\text{remin}}$. The densest water-mass coming from the Southern Ocean
 353 (southern dense water-mass) contribute predominantly to the deep ocean $\text{DIC}_{\text{remin}}$ increase. This water-mass covers a large
 354 portion of the deep ocean, and have particularly strong correlation between spatial fields of AOU trends and ideal-age trends.
 355 While we highlight the importance of change in ideal-age in this water-mass, a substantial portion of the change in AOU is not
 356 driven by change in ideal-age in lighter water-masses. Here, changes in export (Henson et al., 2022), spatially variable oxygen
 357 utilisation rate (Sulpis et al., 2023) or changes in remineralisation with temperature (Brewer and Peltzer, 2017) can de-correlate
 358 changes in AOU from changes in ideal-age. Furthermore, in a transient climate, the conditions (strong advection over mixing

359 and spatially even respiration) for a linear relationship between AOU trends and [ventilation](#) age trends can change over time.
360 Changes in circulation can also recombine ~~water masses~~ differently bringing in waters with varying histories;
361 waters can follow different pathways and go through different respiration fields (Guo et al., 2023). In the lighter ~~water masses~~
362 [water masses](#) and in the Atlantic dense ~~water mass~~[water mass](#), changes in ideal-age explain a slightly smaller portion of the
363 spatial variability of AOU changes in the future compare to the contemporary period (weaker R^2), suggesting caution when
364 interpreting ~~circulation~~ [ventilation](#) changes from AOU.

365 [Our work shows that ESMS have substantially different sensitivities of AOU to ventilation changes, indicating uncertainty.](#)
366 [The models that simulate the strongest slow down of the overturning circulation do not necessarily produce the strongest](#)
367 [increase in AOU \(Liu et al., 2023\), complicating the interpretation of projections of carbon sequestration. Divergent model](#)
368 [sensitivities may reflect different remineralization rate parametrizations \(Maerz et al., 2026; Brabson et al., 2026\), different](#)
369 [organic matter fluxes into the interior \(Henson et al., 2022\) and more generally differences in the representation of marine](#)
370 [biogeochemistry \(S  ferian et al., 2020; Fennel et al., 2022\). The inter-model spread in the sensitivities might also indicate](#)
371 [model dependent spatial distribution of water-masses and the differences in ventilation mechanisms \(mixing, advection\) and](#)
372 [pathways. Additionally, the AOU response could be state dependent, varying with the physical and biogeochemical background](#)
373 [\(e.g., stratification, export production, remineralization depth\).](#)

374 ~~On~~ [One](#) of the initial motivation for this work was to constrain ESM projections of AOU using changes in [ventilation](#) age. Our
375 results suggest that ~~if we can constrain the constraining of~~ deep ocean ventilation changes ~~then we can constrain in ESMS with~~
376 ~~observed ventilation changes (Waugh et al., 2013; Gerke et al., 2024; Wefing et al., 2025; Guo et al., 2026) is a prerequisite for~~
377 ~~constraining~~ projections of deep ocean AOU. However, identifying the best ESMS at projecting deep ocean ventilation changes
378 is challenging. For instance, under a different climate, the last glacial maximum, ESMS simulate very different changes in
379 Atlantic MOC (meridional overturning circulation) depth and strength, and no ESM is consistent with the estimations from
380 proxies (Sherriff-Tadano and Klockmann, 2021). On the other hand, simulated changes in the North Atlantic circulation during
381 stadial-interstadial climate transition show promising comparison with proxy data (Waelbroeck et al., 2023). An accurate
382 projection of the carbon sequestration by the BCP in the deep ocean needs an accurate formation of the deep water-masses
383 in the North Atlantic and Southern Ocean, yet it is not possible to determine even one CMIP6 model that represents those
384 accurately (Heuz  , 2021).

385 Constraining only ~~circulation~~ [ventilation](#) changes may not be enough to identify the best ESMS at projecting changes in AOU
386 in the interior ocean. ~~The sensitivity of AOU changes to age changes varies substantially between ESMS (Fig. 3), modulating~~
387 ~~circulation-driven, since the divergent sensitivities of AOU to ventilation changes modulate ventilation-driven~~ changes in AOU.
388 ~~For instance, the slow-down of the Southern and Atlantic MOC in MPI-ESM1.2-LR is stronger compared to MIROC-ES2L~~
389 ~~(Liu et al., 2023), yet MPI-ESM1.2-LR shows the weakest change in ideal-age-driven AOU trends and MIROC-ES2L the~~
390 ~~strongest one (Fig. 4).~~ The linear relationship between present and future sensitivity across ESMS is promising, in particular
391 in the Southern dense water-mass which covers the largest portion of the deep ocean. It can, in theory, be used to identify
392 ESMS whose sensitivities are the most consistent with observations in the contemporary period and be used to constrain the
393 sensitivity of the future period. However, at this point in time, we cannot directly constrain the sensitivity following an emergent
394 constraint approach (Bourgeois et al., 2022; Kwiatkowski et al., 2017; Goris et al., 2023) because of the small ESM ensemble
395 available and the uncertainties in the observations based estimates. [Improved constraints using oxygen, transient tracers, and](#)
396 [water-mass age diagnostics, alongside particle flux observations, can help evaluate and reduce structural model uncertainties](#)
397 [\(Marsay et al., 2015; DeVries and Primeau, 2011\).](#)

398 The reliability of the $S_{\Delta \text{Age}}^{\Delta \text{AOU}}$ estimates from observational data is compromised by the limited number of data points and the
399 usage of the TTD method for estimating [ventilation](#) age trends. While the scarcity of data and the need to compute trends in
400 T-S space lead to a substantial overestimation when compared to a non-scarce data set, using trends in TTD-mean-age results in
401 an equally strong underestimation when compared to trends computed with ideal-age. While we are confident in our estimate
402 of the first uncertainty, we are more cautious regarding the evaluation of the second uncertainty (TTD method). In the model

403 simulations, in the ocean below 1000 metres, only the Southern Ocean and the North Atlantic are well-ventilated to the degree
404 that the CFC-12 concentrations can provide TTD-mean-age estimates. Thus, we can evaluate trends in TTD-mean-age against
405 trends in ideal-age only in these regions, representing a limited portion of the area covered by the observational dataset. Caution
406 is warranted when using TTD-mean-age to assess changes in ventilation, especially when TTD methods depend on assumptions
407 about the balance between advection and mixing (Δ/Γ). $\Delta/\Gamma = 1$ is a good compromise for the entire ocean but regionally
408 dependent Δ/Γ would lead to more optimal TTD-mean-age when compared to model (He et al., 2018). Approaches employing
409 dual constraint are promising and should be further explored (Guo et al., 2025)(Guo et al., 2025, 2026). While imperfect, the
410 estimates of $S_{\Delta\text{age}}^{\Delta\text{AOU}}$ based on scarce observational data and TTD-mean-age remain the only viable option for comparing $S_{\Delta\text{age}}^{\Delta\text{AOU}}$
411 derived from ESMs. Given that $S_{\Delta\text{age}}^{\Delta\text{AOU}}$ is to some extent similar to an estimation of the oxygen utilisation rate averaged within
412 the water-masses considered, comparison with prior observational-based OUR estimates is appropriate. In the deep ocean,
413 oxygen utilisation rate estimations typically vary around $0.1 \text{ mmol O}_2 \text{ m}^{-3} \text{ yr}^{-1}$ (Sulpis et al., 2023), substantially higher than
414 the observation-based estimates from our work, yet on the lower end of the $S_{\Delta\text{age}}^{\Delta\text{AOU}}$ range derived from ESMs.

415 One caveat of our work is the use of AOU as a proxy of remineralised organic matter, notably as we focus on the deep ocean
416 where water parcels coming from the high latitude can be exported while being-undersaturated with respect to oxygen (Ito
417 et al., 2004; Duteil et al., 2013). Interestingly, when compared to true oxygen utilisation (TOU), which is a more accurate
418 measure of remineralised organic matter, AOU overestimates TOU but changes in AOU underestimates changes in TOU by
419 25 % (Koeve et al., 2020). This uncertainty is also linked to the the physical representation biases in ESMs that strongly affect
420 the projections of interior oxygen changes (Ito et al., 2026), hence AOU. In addition, AOU underestimates organic matter
421 remineralisation because it does not account for denitrification occurring in suboxic waters. In global warming simulations, the
422 volume of suboxic waters increases all along the 20th and 21st century resulting in a small increase in denitrification (Fu et al.,
423 2018; Cocco et al., 2013). Nevertheless, since suboxic waters are mostly located in the upper 1000 metres of the ocean, the
424 omission of denitrification is expected to have a minimal impact on our results. If it does have an impact, it would likely result
425 in a small underestimation of $S_{\Delta\text{age}}^{\Delta\text{AOU}}$. Altogether, this highlights the need to consider the AOU uncertainty when inferred as
426 a proxy for remineralised organic matter in ESMs, calling for getting TOU outputs in future Coupled Model Intercomparison
427 Project in order to properly quantify the projected BCP changes.

428 5 Conclusion

429 Understanding changes in ocean BCP and its impact on future climate change remains an outstanding research question (Tjip-
430 tra et al., 2025). In this work, we have demonstrated that the spatial fields of AOU trends (an indicator of changes in the
431 BCP) and ideal-age trends are correlated in the ocean deeper than 1000 metres. Here, spatial variability in ideal-age trends
432 can explain more than half of the spatial variability in AOU trends ($R^2 \geq 0.5$). This relationship is identified in simulations
433 of the contemporary period (1982-2013) and simulations of the future period (2015-2099) under the SSP5-8.5 climate change
434 scenario. The sensitivity of AOU change to ideal-age change, $S_{\Delta\text{age}}^{\Delta\text{AOU}}$ (that is, the slope of the linear regression), varies between
435 the ESMs and the water-masses from 0.05 to $0.75 \text{ mmol O}_2 \text{ m}^{-3} \text{ yr}^{-1}$ for the contemporary period, depending on the ocean
436 regions. $S_{\Delta\text{age}}^{\Delta\text{AOU}}$ remain relatively similar when computed for the 2015-2099 period. Using the linear relationship we estimate
437 that, for the 2015-2099 time period, the increase in ideal-age, due to changes in ~~circulation or ventilation rates~~ ventilation rates
438 or redistribution of waters, contribute between 43 % and 106 % to the increase in deep ocean $\text{DIC}_{\text{remin}}$, which varies between
439 ESMs.

440 Disparities in deep ocean AOU changes across ESMs stem from differences in ~~circulation-ventilation~~ ventilation changes and differences in
441 the sensitivity of AOU to these ~~circulation-ventilation~~ ventilation changes. Constraining deep ocean AOU changes requires addressing both
442 ~~circulation-ventilation~~ ventilation changes and sensitivities. Constraining sensitivities seems in reach, but would require a greater number of
443 models providing ideal-age and preformed tracers, as well as expanding the observational database and refining the estimation of
444 ventilation age changes from ocean tracers. It is our hope that the ESMs represented in CMIP7 will offer further improvements

445 compared to CMIP6 in terms of their representation of ventilation, especially deep water formation, as well as available outputs
446 in the CMIP7 database. Given a larger model ensemble and more observations, our approach is a promising solution that would
447 allow us to constrain the remineralised carbon sequestration in the deep ocean for the next ESM generations to come. Finally,
448 while ~~circulation-driven~~ ~~ventilation-driven~~ changes in deep ocean carbon sequestration are substantial, they represent only one
449 aspect of the overall process. Changes in biological processes also play a substantial role, particularly in shallower ocean
450 regions. Uncertainties associated to the biological processes driving interior ocean remineralisation in the different models
451 remain (Henson et al., 2024), deserving specific attention to understand carbon sequestration in the intermediate depth ocean.
452 Last but not least, constraining simulated changes in oxygen utilisation will also be ~~on-step-toward~~ ~~one step towards~~ reconciling
453 simulated and observed rates of current deoxygenation (Ito et al., 2026). [Constraining models uncertainties is critical for reliable
454 projections of coupled ocean carbon, and oxygen budgets under climate change.](#)

455 Authors contributions

456 Funding acquisition JT, Conceptualization and methodology DC, NG, SKL, JT, Formal analysis and visualization DC, XD,
457 Analysis of the results DC, XD, NG, EJ, SKL, JT, Writing (original draft preparation) DC, Writing (review and editing) DC,
458 XD, NG, EJ, SKL, JT,

459 Acknowledgements

460 This work was funded by the European Union under grant agreement no. 101083922 (OceanICU) [and UK Research and
461 Innovation \(UKRI\) under the UK government's Horizon Europe funding guarantee \[grant number 10054454, 10063673,
462 10064020, 10059241, 10079684, 10059012, 10048179\]](#). Views and opinions expressed are however those of the author(s)
463 only and do not necessarily reflect those of the European Union or European Research Executive Agency. Neither the Euro-
464 pean Union nor the granting authority can be held responsible for them. [NG acknowledges funding of the Bjerknes Center for
465 Climate Research via the strategic project "The Breathing Ocean". EJ acknowledges funding of the Bjerknes Center for Climate
466 Research via the strategic project "DYNASOR".](#) The computational and storage resources were provided by Sigma2 - the Na-
467 tional Infrastructure for High Performance Computing and Data Storage in Norway (project no. NN1002K, NS1002K). The
468 authors acknowledge the World Climate Research Programme, which, through its Working Group on Coupled Modelling, co-
469 ordinated and promoted CMIP6. ~~The authors~~ [We](#) thank the climate modelling groups for producing and making available their
470 model output, the Earth System Grid Federation (ESGF) for archiving the data and providing access, and the multiple funding
471 agencies who support CMIP6 and ESGF. ~~The authors acknowledge~~ [Support from](#) the KeyCLIM project (grant 295046 from the
472 Research Council of Norway) ~~for coordinating~~, [which coordinated](#) access to the CMIP6 data, [is gratefully acknowledged](#). ~~The
473 authors~~ [We](#) thank the two anonymous reviewers for their valuable feedbacks on the manuscript.

474 Data availability

475 CMIP6 outputs are available from the Earth System Grid Federation (ESGF) portals (e.g. <https://esgf-node.ipsl.upmc.fr>). The
476 observational dataset GLODAPv2 (2016) is available at https://doi.org/10.3334/cdiac/otg.ndp093_glodapv2 and the ~~water-mass
477 ventilation~~ [ages](#) product at <https://doi.org/10.25921/xp33-q351> (Lauvset et al., 2023; Jeansson et al., 2021).

Code availability

The code for producing the figure is available at <https://github.com/damiencouespel/scripts-article-biological-carbon-pump-aou-trends-vs-age-trends>.

Competing interests

The authors declare no competing interests.

References

- L. A. Anderson and J. L. Sarmiento. Redfield ratios of remineralization determined by nutrient data analysis. *Global Biogeochemical Cycles*, 8(1):65–80, 1994. ISSN 1944-9224. doi: 10.1029/93GB03318.
- L. Bopp, L. Resplandy, A. Untersee, P. Le Mezo, and M. Kageyama. Ocean (de)oxygenation from the Last Glacial Maximum to the 21st century: Insights from Earth System Models. *Philosophical Transactions of the Royal Society A: Mathematical, Physical and Engineering Sciences*, 375(2102), 2017. doi: 10.1098/rsta.2016.0323.
- O. Boucher, J. Servonnat, A. L. Albright, O. Aumont, Y. Balkanski, V. Bastrikov, S. Bekki, R. Bonnet, S. Bony, L. Bopp, P. Braconnot, P. Brockmann, P. Cadule, A. Caubel, F. Cheruy, F. Codron, A. Cozic, D. Cugnet, F. D’Andrea, P. Davini, C. de Lavergne, S. Denvil, J. Deshayes, M. Devilliers, A. Ducharne, J.-L. Dufresne, E. Dupont, C. Éthé, L. Fairhead, L. Falletti, S. Flavoni, M.-A. Foujols, S. Gardoll, G. Gastineau, J. Ghattas, J.-Y. Grandpeix, B. Guenet, E. Guez, Lionel, E. Guilyardi, M. Guimberteau, D. Hauglustaine, F. Hourdin, A. Idelkadi, S. Joussaume, M. Kageyama, M. Khodri, G. Krinner, N. Lebas, G. Levavasseur, C. Lévy, L. Li, F. Lott, T. Lurton, S. Luysaert, G. Madec, J.-B. Madeleine, F. Maignan, M. Marchand, O. Marti, L. Mellul, Y. Meurdesoif, J. Mignot, I. Musat, C. Ottlé, P. Peylin, Y. Planton, J. Polcher, C. Rio, N. Rochetin, C. Rousset, P. Sepulchre, A. Sima, D. Swingedouw, R. Thiéblemont, A. K. Traore, M. Vancoppenolle, J. Vial, J. Vialard, N. Viovy, and N. Vuichard. Presentation and Evaluation of the IPSL-CM6A-LR Climate Model. *Journal of Advances in Modeling Earth Systems*, 12(7):e2019MS002010, 2020. ISSN 1942-2466. doi: 10.1029/2019MS002010.
- T. Bourgeois, N. Goris, J. Schwinger, and J. F. Tjiputra. Stratification constrains future heat and carbon uptake in the Southern Ocean between 30°S and 55°S. *Nature Communications*, 13(1):340, Jan. 2022. ISSN 2041-1723. doi: 10.1038/s41467-022-27979-5.
- P. W. Boyd, H. Claustre, M. Lévy, D. A. Siegel, and T. Weber. Multi-faceted particle pumps drive carbon sequestration in the ocean. *Nature*, 568(7752):327–335, Apr. 2019. ISSN 0028-0836. doi: 10.1038/s41586-019-1098-2.
- E. K. Brabson, L. F. Doyle, R. P. Acosta, A. V. Fedorov, P. M. Hull, and N. J. Burls. A revised temperature-dependent remineralization scheme for the Community Earth System Model (v1.2.2). *Geoscientific Model Development*, 19(3):1143–1156, Feb. 2026. ISSN 1991-959X. doi: 10.5194/gmd-19-1143-2026.
- P. G. Brewer and E. T. Peltzer. Depth perception: The need to report ocean biogeochemical rates as functions of temperature, not depth. *Philosophical Transactions of the Royal Society A: Mathematical, Physical and Engineering Sciences*, 375(2102):20160319, Aug. 2017. doi: 10.1098/rsta.2016.0319.
- W. S. Broecker, S. Blanton, W. M. Smethie Jr., and G. Ostlund. Radiocarbon decay and oxygen utilization in the Deep Atlantic Ocean. *Global Biogeochemical Cycles*, 5(1):87–117, 1991. ISSN 1944-9224. doi: 10.1029/90GB02279.

- 512 W. S. Broecker, S. L. Peacock, S. Walker, R. Weiss, E. Fahrbach, M. Schroeder, U. Mikolajewicz, C. Heinze, R. Key, T.-H.
513 Peng, and S. Rubin. How much deep water is formed in the Southern Ocean? *Journal of Geophysical Research: Oceans*,
514 103(C8):15833–15843, 1998. ISSN 2156-2202. doi: 10.1029/98JC00248.
- 515 R. Caneill and A. Barna. Gsw-xarray. Zenodo, May 2024.
- 516 V. Cocco, F. Joos, M. Steinacher, T. L. Frölicher, L. Bopp, J. P. Dunne, M. Gehlen, C. Heinze, J. Orr, A. Oschlies, B. Schneider,
517 J. Segschneider, and J. Tjiputra. Oxygen and indicators of stress for marine life in multi-model global warming projections.
518 *Biogeosciences*, 10(3):1849–1868, 2013. doi: 10.5194/bg-10-1849-2013.
- 519 C. Deutsch, H. Brix, T. Ito, H. Frenzel, and L. Thompson. Climate-forced variability of ocean hypoxia. *Science*, 333(6040):
520 336–339, 2011. doi: 10.1126/science.1202422.
- 521 T. DeVries. The Ocean Carbon Cycle. *Annual Review of Environment and Resources*, 47(1):317–341, 2022. doi:
522 10.1146/annurev-environ-120920-111307.
- 523 T. DeVries and F. Primeau. Dynamically and Observationally Constrained Estimates of Water-Mass Distributions and Ages in
524 the Global Ocean. *Journal of Physical Oceanography*, 41(12):2381–2401, Dec. 2011. ISSN 0022-3670, 1520-0485. doi:
525 10.1175/JPO-D-10-05011.1.
- 526 J. P. Dunne, L. W. Horowitz, A. J. Adcroft, P. Ginoux, I. M. Held, J. G. John, J. P. Krasting, S. Malyshev, V. Naik, F. Paulot,
527 E. Shevliakova, C. A. Stock, N. Zadeh, V. Balaji, C. Blanton, K. A. Dunne, C. Dupuis, J. Durachta, R. Dussin, P. P. G.
528 Gauthier, S. M. Griffies, H. Guo, R. W. Hallberg, M. Harrison, J. He, W. Hurlin, C. McHugh, R. Menzel, P. C. D. Milly,
529 S. Nikonov, D. J. Paynter, J. Ploshay, A. Radhakrishnan, K. Rand, B. G. Reichl, T. Robinson, D. M. Schwarzkopf, L. T.
530 Sentman, S. Underwood, H. Vahlenkamp, M. Winton, A. T. Wittenberg, B. Wyman, Y. Zeng, and M. Zhao. The GFDL Earth
531 System Model Version 4.1 (GFDL-ESM 4.1): Overall Coupled Model Description and Simulation Characteristics. *Journal*
532 *of Advances in Modeling Earth Systems*, 12(11):e2019MS002015, 2020. ISSN 1942-2466. doi: 10.1029/2019MS002015.
- 533 O. Duteil, W. Koeve, A. Oschlies, D. Bianchi, E. Galbraith, I. Kriest, and R. Matear. A novel estimate of ocean oxygen
534 utilisation points to a reduced rate of respiration in the ocean interior. *Biogeosciences*, 10(11):7723–7738, Nov. 2013. ISSN
535 1726-4170. doi: 10.5194/bg-10-7723-2013.
- 536 R. A. Feely, C. L. Sabine, R. Schlitzer, J. L. Bullister, S. Mecking, and D. Greeley. Oxygen Utilization and Organic Carbon
537 Remineralization in the Upper Water Column of the Pacific Ocean. *Journal of Oceanography*, 60(1):45–52, Feb. 2004. ISSN
538 1573-868X. doi: 10.1023/B:JOCE.0000038317.01279.aa.
- 539 K. Fennel, J. P. Mattern, S. C. Doney, L. Bopp, A. M. Moore, B. Wang, and L. Yu. Ocean biogeochemical modelling. *Nature*
540 *Reviews Methods Primers*, 2(1):76, Sept. 2022. ISSN 2662-8449. doi: 10.1038/s43586-022-00154-2.
- 541 I. Frenger, A. Landolfi, K. Kvale, C. J. Somes, A. Oschlies, W. Yao, and W. Koeve. Misconceptions of the marine biological
542 carbon pump in a changing climate: Thinking outside the “export” box. *Global Change Biology*, 30(1):e17124, 2024. ISSN
543 1365-2486. doi: 10.1111/gcb.17124.
- 544 W. Fu, F. Primeau, J. Keith Moore, K. Lindsay, and J. T. Randerson. Reversal of increasing tropical ocean hypoxia trends with
545 sustained climate warming. *Global Biogeochemical Cycles*, 32(4):551–564, 2018. doi: 10.1002/2017GB005788.
- 546 H. Garcia and L. Gordon. Erratum: Oxygen solubility in seawater: Better fitting equations. *Limnology and Oceanography*, 38:
547 656, 1993.
- 548 H. E. Garcia and L. I. Gordon. Oxygen solubility in seawater: Better fitting equations. *Limnology and Oceanography*, 37(6):
549 1307–1312, 1992. doi: 10.4319/lo.1992.37.6.1307.

- 550 H. E. Garcia, Z. Wang, C. Bouchard, S. L. Cross, C. R. Paver, J. R. Reagan, T. P. Boyer, R. A. Locarnini, A. V. Mishonov,
551 O. K. Baranova, D. Seidov, and D. Dukhovskoy. World Ocean Atlas 2023, Volume 3: Dissolved Oxygen, Apparent Oxygen
552 Utilization, Dissolved Oxygen Saturation and 30-year Climate Normal. A. Mishonov Technical Editor. *NOAA Atlas NESDIS*
553 *91*, 2024. doi: 10.25923/rb67-ns53.
- 554 L. Gerke, Y. Arck, and T. Tanhua. Temporal Variability of Ventilation in the Eurasian Arctic Ocean. *Journal of Geophysical*
555 *Research: Oceans*, 129(7):e2023JC020608, 2024. ISSN 2169-9291. doi: 10.1029/2023JC020608.
- 556 P. Goodwin, M. J. Follows, and R. G. Williams. Analytical relationships between atmospheric carbon dioxide, carbon emissions,
557 and ocean processes. *Global Biogeochemical Cycles*, 22(3), 2008. ISSN 1944-9224. doi: 10.1029/2008GB003184.
- 558 N. Goris, K. Johannsen, and J. Tjiputra. The emergence of the Gulf Stream and interior western boundary as key regions to
559 constrain the future North Atlantic carbon uptake. *Geoscientific Model Development*, 16(8):2095–2117, Apr. 2023. ISSN
560 1991-959X. doi: 10.5194/gmd-16-2095-2023.
- 561 H. Guo, I. Kriest, A. Oschlies, and W. Koeve. Can Oxygen Utilization Rate Be Used to Track the Long-Term Changes of
562 Aerobic Respiration in the Mesopelagic Atlantic Ocean? *Geophysical Research Letters*, 50(13):e2022GL102645, 2023.
563 ISSN 1944-8007. doi: 10.1029/2022GL102645.
- 564 H. Guo, W. Koeve, A. Oschlies, Y.-C. He, T. P. Kemena, L. Gerke, and I. Kriest. Dual-tracer constraints on the inverse Gaussian
565 transit time distribution improve the estimation of water mass ages and their temporal trends in the tropical thermocline.
566 *Ocean Science*, 21(3):1167–1182, July 2025. ISSN 1812-0784. doi: 10.5194/os-21-1167-2025.
- 567 H. Guo, W. Koeve, I. Kriest, I. Frenger, T. Tanhua, P. Brandt, Y. He, T. Xue, and A. Oschlies. North Atlantic ventilation change
568 over the past three decades is potentially driven by climate change. *Nature Communications*, 17(1):200, Jan. 2026. ISSN
569 2041-1723. doi: 10.1038/s41467-025-67923-x.
- 570 T. Hajima, M. Watanabe, A. Yamamoto, H. Tatebe, M. A. Noguchi, M. Abe, R. Ohgaito, A. Ito, D. Yamazaki, H. Okajima,
571 A. Ito, K. Takata, K. Ogochi, S. Watanabe, and M. Kawamiya. Development of the MIROC-ES2L Earth system model and
572 the evaluation of biogeochemical processes and feedbacks. *Geoscientific Model Development*, 13(5):2197–2244, May 2020.
573 ISSN 1991-959X. doi: 10.5194/gmd-13-2197-2020.
- 574 Y.-C. He, J. Tjiputra, H. R. Langehaug, E. Jeansson, Y. Gao, J. Schwinger, and A. Olsen. A Model-Based Evaluation of the
575 Inverse Gaussian Transit-Time Distribution Method for Inferring Anthropogenic Carbon Storage in the Ocean. *Journal of*
576 *Geophysical Research: Oceans*, 123(3):1777–1800, Mar. 2018. ISSN 2169-9275, 2169-9291. doi: 10.1002/2017jc013504.
- 577 S. Henson, C. A. Baker, P. Halloran, A. McQuatters-Gollop, S. Painter, A. Planchat, and A. Tagliabue. Knowledge Gaps
578 in Quantifying the Climate Change Response of Biological Storage of Carbon in the Ocean. *Earth's Future*, 12(6):
579 e2023EF004375, 2024. ISSN 2328-4277. doi: 10.1029/2023EF004375.
- 580 S. A. Henson, C. Laufkötter, S. Leung, S. L. C. Giering, H. I. Palevsky, and E. L. Cavan. Uncertain response of ocean biological
581 carbon export in a changing world. *Nature Geoscience*, 15(4):248–254, Apr. 2022. ISSN 1752-0908. doi: 10.1038/s41561-
582 022-00927-0.
- 583 C. Heuzé. Antarctic Bottom Water and North Atlantic Deep Water in CMIP6 models. *Ocean Science*, 17(1):59–90, Jan. 2021.
584 ISSN 1812-0784. doi: 10.5194/os-17-59-2021.
- 585 T. Ito, M. J. Follows, and E. A. Boyle. Is AOU a good measure of respiration in the oceans? *Geophysical Research Letters*, 31
586 (17), 2004. ISSN 1944-8007. doi: 10.1029/2004GL020900.
- 587 T. Ito, Y. Takano, Y. A. Eddebbbar, J. F. Tiputra, Z. Wang, S. Minobe, L. Cheng, J. Du, and Y. Abe. Are Simulated Ocean
588 Deoxygenation Rates Consistent with the Observational Reconstructions? *Annual Review Earth and Planetary Sciences*,
589 Jan. 2026. doi: 10.1146/annurev-earth-032524-123111.

- 590 E. Jeansson, R. Steinfeldt, and T. Toste. Water mass ages based on GLODAPv2 data product (NCEI Accession 0226793).
591 NOAA National Centers for Environmental Information., 2021.
- 592 E. Jeansson, T. Tanhua, A. Olsen, W. M. Smethie Jr., B. Rajasakaren, S. R. Ólafsdóttir, and J. Ólafsson. Decadal Changes in Ven-
593 tilation and Anthropogenic Carbon in the Nordic Seas. *Journal of Geophysical Research: Oceans*, 128(3):e2022JC019318,
594 2023. ISSN 2169-9291. doi: 10.1029/2022JC019318.
- 595 W. J. Jenkins. Oxygen utilization rates in North Atlantic subtropical gyre and primary production in oligotrophic systems.
596 *Nature*, 300(5889):246–248, Nov. 1982. ISSN 1476-4687. doi: 10.1038/300246a0.
- 597 R. F. Keeling, A. Körtzinger, and N. Gruber. Ocean deoxygenation in a warming world. *Annual review of marine science*, 2:
598 199–229, 2010. doi: 10.1146/annurev.marine.010908.163855.
- 599 A. Kessler, E. V. Galaasen, U. S. Ninnemann, and J. Tjiputra. Ocean carbon inventory under warmer climate conditions – the
600 case of the Last Interglacial. *Climate of the Past*, 14(12):1961–1976, Dec. 2018. ISSN 1814-9324. doi: 10.5194/cp-14-1961-
601 2018.
- 602 R. M. Key, A. Olsen, S. van Heuven, S. K. Lauvset, A. Velo, X. Lin, C. Schirnick, A. Kozyr, T. Tanhua, M. Hoppema,
603 S. Jutterström, R. Steinfeldt, E. Jeansson, M. Ishii, F. F. Pérez, and T. Suzuki. Global Ocean Data Analysis Project, Version
604 2 (GLODAPv2), ORNL/CDIAC-162, NDP-093. Technical report, Carbon Dioxide Information Analysis Center, Oak Ridge
605 National Laboratory, US Department of Energy, Oak Ridge, Tennessee., 2015.
- 606 W. Koeve and P. Kähler. Oxygen utilization rate (OUR) underestimates ocean respiration: A model study. *Global Biogeochem-*
607 *ical Cycles*, 30(8):1166–1182, 2016. ISSN 1944-9224. doi: 10.1002/2015GB005354.
- 608 W. Koeve, P. Kähler, and A. Oschlies. Does Export Production Measure Transient Changes of the Biological Carbon Pump’s
609 Feedback to the Atmosphere Under Global Warming? *Geophysical Research Letters*, 47(22):e2020GL089928, 2020. ISSN
610 1944-8007. doi: 10.1029/2020GL089928.
- 611 L. Kwiatkowski, L. Bopp, O. Aumont, P. Ciais, P. M. Cox, C. Laufkötter, Y. Li, and R. Séférian. Emergent constraints on
612 projections of declining primary production in the tropical oceans. *Nature Climate Change*, 7(5):355–358, May 2017. ISSN
613 17586798. doi: 10.1038/nclimate3265.
- 614 L. Kwiatkowski, O. Torres, L. Bopp, O. Aumont, M. Chamberlain, J. R. Christian, J. P. Dunne, M. Gehlen, T. Ilyina, J. G.
615 John, A. Lenton, H. Li, N. S. Lovenduski, J. C. Orr, J. Palmieri, Y. Santana-Falcón, J. Schwinger, R. Séférian, C. A. Stock,
616 A. Tagliabue, Y. Takano, J. Tjiputra, K. Toyama, H. Tsujino, M. Watanabe, A. Yamamoto, A. Yool, and T. Ziehn. Twenty-first
617 century ocean warming, acidification, deoxygenation, and upper-ocean nutrient and primary production decline from CMIP6
618 model projections. *Biogeosciences*, 17(13):3439–3470, July 2020. ISSN 1726-4189. doi: 10.5194/bg-17-3439-2020.
- 619 E. Y. Kwon, F. Primeau, and J. L. Sarmiento. The impact of remineralization depth on the air–sea carbon balance. *Nature*
620 *Geoscience*, 2(9):630–635, Sept. 2009. ISSN 1752-0908. doi: 10.1038/ngeo612.
- 621 S. K. Lauvset, R. M. Key, A. Olsen, S. M. A. C. van Heuven, A. Velo, X. Lin, C. Schirnick, A. Kozyr, T. Tanhua, M. Hoppema,
622 S. Jutterström, R. Steinfeldt, E. Jeansson, M. Ishii, F. F. Pérez, T. Suzuki, and S. Watelet. A new global interior ocean mapped
623 climatology: The 1° × 1° GLODAP version 2 from 1972-01-01 to 2013-12-31 (NCEI Accession 0286118). NOAA National
624 Centers for Environmental Information. Dataset., 2023.
- 625 S. K. Lauvset, N. Lange, T. Tanhua, H. C. Bittig, A. Olsen, A. Kozyr, M. Álvarez, K. Azetsu-Scott, P. J. Brown, B. R. Carter,
626 L. Cotrim da Cunha, M. Hoppema, M. P. Humphreys, M. Ishii, E. Jeansson, A. Murata, J. D. Müller, F. F. Pérez, C. Schirnick,
627 R. Steinfeldt, T. Suzuki, A. Ulfsbo, A. Velo, R. J. Woosley, and R. M. Key. The annual update GLODAPv2.2023: The global
628 interior ocean biogeochemical data product. *Earth System Science Data*, 16(4):2047–2072, Apr. 2024. ISSN 1866-3508.
629 doi: 10.5194/essd-16-2047-2024.

- 630 Y. Liu and F. Primeau. Surface-to-Interior Transport Timescales and Ventilation Patterns in a Time-Dependent Circulation
631 Driven by Sustained Climate Warming. *Journal of Physical Oceanography*, 54(1):173–186, Dec. 2023. ISSN 0022-3670,
632 1520-0485. doi: 10.1175/JPO-D-23-0113.1.
- 633 Y. Liu, J. K. Moore, F. Primeau, and W. L. Wang. Reduced CO₂ uptake and growing nutrient sequestration from slowing
634 overturning circulation. *Nature Climate Change*, 13(1):83–90, Jan. 2023. ISSN 1758-6798. doi: 10.1038/s41558-022-
635 01555-7.
- 636 J. Maerz, K. D. Six, S. Ahmerkamp, and T. Ilyina. Marine particles and their remineralization buffer future ocean biogeochem-
637 istry response to climate warming. *Biogeosciences*, 23(5):1897–1929, Mar. 2026. ISSN 1726-4170. doi: 10.5194/bg-23-
638 1897-2026.
- 639 E. Maier-Reimer, U. Mikolajewicz, and A. Winguth. Future ocean uptake of CO₂: Interaction between ocean circulation and
640 biology. *Climate Dynamics*, 12(10):711–721, 1996. ISSN 09307575. doi: 10.1007/s003820050138.
- 641 I. Marinov, A. Gnanadesikan, J. L. Sarmiento, J. R. Toggweiler, M. Follows, and B. K. Mignone. Impact of oceanic circulation
642 on biological carbon storage in the ocean and atmospheric pCO₂. *Global Biogeochemical Cycles*, 22(3):GB3007—n/a,
643 2008. doi: 10.1029/2007GB002958.
- 644 C. M. Marsay, R. J. Sanders, S. A. Henson, K. Pabortsava, E. P. Achterberg, and R. S. Lampitt. Attenuation of sinking
645 particulate organic carbon flux through the mesopelagic ocean. *Proceedings of the National Academy of Sciences*, 112(4):
646 1089–1094, Jan. 2015. doi: 10.1073/pnas.1415311112.
- 647 T. Mauritsen, J. Bader, T. Becker, J. Behrens, M. Bittner, R. Brokopf, V. Brovkin, M. Claussen, T. Crueger, M. Esch, I. Fast,
648 S. Fiedler, D. Fläschner, V. Gayler, M. Giorgetta, D. S. Goll, H. Haak, S. Hagemann, C. Hedemann, C. Hohenegger, T. Ily-
649 ina, T. Jahns, D. Jimenéz-de-la-Cuesta, J. Jungclaus, T. Kleinen, S. Kloster, D. Kracher, S. Kinne, D. Kleberg, G. Lass-
650 lop, L. Kornbluh, J. Marotzke, D. Matei, K. Meraner, U. Mikolajewicz, K. Modali, B. Möbis, W. A. Müller, J. E. M. S.
651 Nabel, C. C. W. Nam, D. Notz, S.-S. Nyawira, H. Paulsen, K. Peters, R. Pincus, H. Pohlmann, J. Pongratz, M. Popp,
652 T. J. Raddatz, S. Rast, R. Redler, C. H. Reick, T. Rohrschneider, V. Schemann, H. Schmidt, R. Schnur, U. Schulzweida,
653 K. D. Six, L. Stein, I. Stemmler, B. Stevens, J.-S. von Storch, F. Tian, A. Voigt, P. Vrese, K.-H. Wieners, S. Wilkenskjaeld,
654 A. Winkler, and E. Roeckner. Developments in the MPI-M Earth System Model version 1.2 (MPI-ESM1.2) and Its Re-
655 sponse to Increasing CO₂. *Journal of Advances in Modeling Earth Systems*, 11(4):998–1038, 2019. ISSN 1942-2466. doi:
656 10.1029/2018MS001400.
- 657 T. J. McDougall and P. M. Barker. *Getting Started with TEOS-10 and the Gibbs Seawater (GSW) Oceanographic Toolbox*.
658 SCOR/IAPSO WG127, 2011. ISBN 978-0-646-55621-5.
- 659 M. S. Myksovoll, A. Britt Sandø, J. Tjiputra, A. Samuelsen, V. Çağlar Yumruktepe, C. Li, E. A. Mousing, J. P. H. Betten-
660 court, and G. Ottersen. Key physical processes and their model representation for projecting climate impacts on subarctic
661 Atlantic net primary production: A synthesis. *Progress in Oceanography*, 217:103084, Sept. 2023. ISSN 0079-6611. doi:
662 10.1016/j.pocean.2023.103084.
- 663 A. Olsen, R. M. Key, S. van Heuven, S. K. Lauvset, A. Velo, X. Lin, C. Schirnick, A. Kozyr, T. Tanhua, M. Hoppema,
664 S. Jutterström, R. Steinfeldt, E. Jeansson, M. Ishii, F. F. Pérez, and T. Suzuki. The Global Ocean Data Analysis Project
665 version 2 (GLODAPv2) – an internally consistent data product for the world ocean. *Earth System Science Data*, 8(2):
666 297–323, Aug. 2016. ISSN 1866-3508. doi: 10.5194/essd-8-297-2016.
- 667 J. L. Sarmiento and J. R. Toggweiler. A new model for the role of the oceans in determining atmospheric P CO₂. *Nature*, 308
668 (5960):621–624, Apr. 1984. ISSN 1476-4687. doi: 10.1038/308621a0.
- 669 J. L. Sarmiento, G. Thiele, R. M. Key, and W. S. Moore. Oxygen and nitrate new production and remineralization in the North
670 Atlantic subtropical gyre. *Journal of Geophysical Research: Oceans*, 95(C10):18303–18315, 1990. ISSN 2156-2202. doi:
671 10.1029/JC095iC10p18303.

- 672 R. S  f  rian, P. Nabat, M. Michou, D. Saint-Martin, A. Voldoire, J. Colin, B. Decharme, C. Delire, S. Berthet, M. Chevallier,
673 S. S  n  si, L. Franchisteguy, J. Vial, M. Mallet, E. Joetzjer, O. Geoffroy, J.-F. Gu  r  my, M.-P. Moine, R. Msadek, A. Ribes,
674 M. Rocher, R. Roehrig, D. Salas-y-M  lia, E. Sanchez, L. Terray, S. Valcke, R. Waldman, O. Aumont, L. Bopp, J. Deshayes,
675 C.   th  , and G. Madec. Evaluation of CNRM Earth System Model, CNRM-ESM2-1: Role of Earth System Processes in
676 Present-Day and Future Climate. *Journal of Advances in Modeling Earth Systems*, 11(12):4182–4227, 2019. ISSN 1942-
677 2466. doi: 10.1029/2019MS001791.
- 678 R. S  f  rian, S. Berthet, A. Yool, J. Palmi  ri, L. Bopp, A. Tagliabue, L. Kwiatkowski, O. Aumont, J. Christian, J. Dunne,
679 M. Gehlen, T. Ilyina, J. G. John, H. Li, M. C. Long, J. Y. Luo, H. Nakano, A. Romanou, J. Schwinger, C. Stock, Y. Santana-
680 Falc  n, Y. Takano, J. Tjiputra, H. Tsujino, M. Watanabe, T. Wu, F. Wu, and A. Yamamoto. Tracking improvement in
681 simulated marine biogeochemistry between CMIP5 and CMIP6. *Current Climate Change Reports*, 6(3):95–119, Aug. 2020.
682 ISSN 2198-6061. doi: 10.1007/s40641-020-00160-0.
- 683   . Seland, M. Bentsen, D. Oliv  ie, T. Toniazzo, A. Gjermundsen, L. S. Graff, J. B. Debernard, A. K. Gupta, Y.-C. He,
684 A. Kirkev  g, J. Schwinger, J. Tjiputra, K. S. Aas, I. Bethke, Y. Fan, J. Griesfeller, A. Grini, C. Guo, M. Ilicak, I. H. H.
685 Karset, O. Landgren, J. Liakka, K. O. Moseid, A. Nummelin, C. Spensberger, H. Tang, Z. Zhang, C. Heinze, T. Iversen,
686 and M. Schulz. Overview of the Norwegian Earth System Model (NorESM2) and key climate response of CMIP6 DECK,
687 historical, and scenario simulations. *Geoscientific Model Development*, 13(12):6165–6200, Dec. 2020. ISSN 1991-959X.
688 doi: 10.5194/gmd-13-6165-2020.
- 689 A. A. Sellar, J. Walton, C. G. Jones, R. Wood, N. L. Abraham, M. Andrejczuk, M. B. Andrews, T. Andrews, A. T. Archibald,
690 L. de Mora, H. Dyson, M. Elkington, R. Ellis, P. Florek, P. Good, L. Gohar, S. Haddad, S. C. Hardiman, E. Hogan, A. Iwi,
691 C. D. Jones, B. Johnson, D. I. Kelley, J. Kettleborough, J. R. Knight, M. O. K  hler, T. Kuhlbrodt, S. Liddicoat, I. Linova-
692 Pavlova, M. S. Mizielski, O. Morgenstern, J. Mulcahy, E. Neinger, F. M. O’Connor, R. Petrie, J. Ridley, J.-C. Rioual,
693 M. Roberts, E. Robertson, S. Rumbold, J. Seddon, H. Shepherd, S. Shim, A. Stephens, J. C. Teixeira, Y. Tang, J. Williams,
694 A. Wiltshire, and P. T. Griffiths. Implementation of U.K. Earth System Models for CMIP6. *Journal of Advances in Modeling*
695 *Earth Systems*, 12(4):e2019MS001946, 2020. ISSN 1942-2466. doi: 10.1029/2019MS001946.
- 696 S. Sherriff-Tadano and M. Klockmann. PMIP contributions to understanding the deep ocean circulation of the Last Glacial Max-
697 imum. *Past Global Changes Magazine*, 29(2):84–85, Nov. 2021. ISSN 2411605X, 24119180. doi: 10.22498/pages.29.2.84.
- 698 R. E. Sonnerup, S. Mecking, J. L. Bullister, and M. J. Warner. Transit time distributions and oxygen utilization rates from
699 chlorofluorocarbons and sulfur hexafluoride in the Southeast Pacific Ocean. *Journal of Geophysical Research: Oceans*, 120
700 (5):3761–3776, 2015. ISSN 2169-9291. doi: 10.1002/2015JC010781.
- 701 O. Sulpis, D. S. Trossman, M. Holzer, E. Jeansson, S. K. Lauvset, and J. J. Middelburg. Respiration Patterns in the Dark Ocean.
702 *Global Biogeochemical Cycles*, 37(8):e2023GB007747, 2023. ISSN 1944-9224. doi: 10.1029/2023GB007747.
- 703 N. C. Swart, J. N. S. Cole, V. V. Kharin, M. Lazare, J. F. Scinocca, N. P. Gillett, J. Anstey, V. Arora, J. R. Christian, S. Hanna,
704 Y. Jiao, W. G. Lee, F. Majaess, O. A. Saenko, C. Seiler, C. Seinen, A. Shao, M. Sigmund, L. Solheim, K. von Salzen, D. Yang,
705 and B. Winter. The Canadian Earth System Model version 5 (CanESM5.0.3). *Geoscientific Model Development*, 12(11):
706 4823–4873, Nov. 2019. ISSN 1991-959X. doi: 10.5194/gmd-12-4823-2019.
- 707 A. Tagliabue, L. Kwiatkowski, L. Bopp, M. Butensch  n, W. Cheung, M. Lengaigne, and J. Vialard. Persistent Uncertainties in
708 Ocean Net Primary Production Climate Change Projections at Regional Scales Raise Challenges for Assessing Impacts on
709 Ecosystem Services. *Frontiers in Climate*, 3:738224, Nov. 2021. ISSN 2624-9553. doi: 10.3389/fclim.2021.738224.
- 710 J. L. Thomas, D. W. Waugh, and A. Gnanadesikan. Relationship between Age and Oxygen along Line W in the Northwest
711 Atlantic Ocean. *Ocean Science Journal*, 55(2):203–217, June 2020. ISSN 1738-5261, 2005-7172. doi: 10.1007/s12601-
712 020-0019-5.

- 713 J. F. Tjiputra, N. Goris, S. K. Lauvset, C. Heinze, A. Olsen, J. Schwinger, and R. Steinfeldt. Mechanisms and Early Detections
714 of Multidecadal Oxygen Changes in the Interior Subpolar North Atlantic. *Geophysical Research Letters*, 45(9):4218–4229,
715 2018. ISSN 1944-8007. doi: 10.1029/2018GL077096.
- 716 J. F. Tjiputra, J. Schwinger, M. Bentsen, A. L. Morée, S. Gao, I. Bethke, C. Heinze, N. Goris, A. Gupta, Y.-C. He, D. Olivie,
717 Ø. Seland, and M. Schulz. Ocean biogeochemistry in the Norwegian Earth System Model version 2 (NorESM2). *Geoscientific Model Development*, 13(5):2393–2431, May 2020. ISSN 1991-959X. doi: 10.5194/gmd-13-2393-2020.
- 719 J. F. Tjiputra, D. Couespel, and R. Sanders. Marine ecosystem role in setting up preindustrial and future climate. *Nature*
720 *Communications*, 16(1):1–8, Mar. 2025. ISSN 2041-1723. doi: 10.1038/s41467-025-57371-y.
- 721 P. Virtanen, R. Gommers, T. E. Oliphant, M. Haberland, T. Reddy, D. Cournapeau, E. Burovski, P. Peterson, W. Weckesser,
722 J. Bright, S. J. van der Walt, M. Brett, J. Wilson, K. J. Millman, N. Mayorov, A. R. J. Nelson, E. Jones, R. Kern, E. Larson,
723 C. J. Carey, Í. Polat, Y. Feng, E. W. Moore, J. VanderPlas, D. Laxalde, J. Perktold, R. Cimrman, I. Henriksen, E. A. Quintero,
724 C. R. Harris, A. M. Archibald, A. H. Ribeiro, F. Pedregosa, and P. van Mulbregt. SciPy 1.0: Fundamental algorithms for
725 scientific computing in Python. *Nature Methods*, 17(3):261–272, Mar. 2020. ISSN 1548-7105. doi: 10.1038/s41592-019-
726 0686-2.
- 727 T. Volk and M. I. Hoffert. Ocean carbon pumps: Analysis of relative strengths and efficiencies in ocean-driven atmospheric
728 CO₂ changes. *The Carbon Cycle and Atmospheric CO₂: Natural Variations Archean to Present*. (1985), 32:99–110, 1985.
729 doi: 10.1029/GM032p0099.
- 730 C. Waelbroeck, J. Tjiputra, C. Guo, K. H. Nisancioglu, E. Jansen, N. Vázquez Riveiros, S. Toucanne, F. Eynaud, L. Rossignol,
731 F. Dewilde, E. Marchès, S. Lebreiro, and S. Nave. Atlantic circulation changes across a stadial–interstadial transition.
732 *Climate of the Past*, 19(5):901–913, May 2023. ISSN 1814-9324. doi: 10.5194/cp-19-901-2023.
- 733 D. W. Waugh, F. Primeau, T. DeVries, and M. Holzer. Recent Changes in the Ventilation of the Southern Oceans. *Science*, 339
734 (6119):568–570, Feb. 2013. doi: 10.1126/science.1225411.
- 735 A.-M. Wefing, A. Payne, M. Scheiwiller, C. Vockenhuber, M. Christl, T. Tanhua, and N. Casacuberta. Changes in water mass
736 composition and circulation in the central Arctic Ocean between 2011 and 2021 inferred from tracer observations. *Ocean*
737 *Science*, 21(6):3311–3340, Dec. 2025. ISSN 1812-0784. doi: 10.5194/os-21-3311-2025.
- 738 W. Weijer, W. Cheng, O. A. Garuba, A. Hu, and B. T. Nadiga. CMIP6 Models Predict Significant 21st Century Decline
739 of the Atlantic Meridional Overturning Circulation. *Geophysical Research Letters*, 47(12):e2019GL086075, 2020. ISSN
740 1944-8007. doi: 10.1029/2019GL086075.
- 741 J. D. Wilson, O. Andrews, A. Katavouta, F. de Melo Viríssimo, R. M. Death, M. Adloff, C. A. Baker, B. Blackledge, F. W.
742 Goldsworth, A. T. Kennedy-Asser, Q. Liu, K. R. Sieradzan, E. Vosper, and R. Ying. The biological carbon pump in CMIP6
743 models: 21st century trends and uncertainties. *Proceedings of the National Academy of Sciences*, 119(29):e2204369119,
744 July 2022. doi: 10.1073/pnas.2204369119.
- 745 T. Ziehn, M. A. Chamberlain, R. M. Law, A. Lenton, R. W. Bodman, M. Dix, L. Stevens, Y.-P. Wang, and J. Srbinovsky.
746 The Australian Earth System Model: ACCESS-ESM1.5. *Journal of Southern Hemisphere Earth Systems Science*, 70(1):
747 193–214, Aug. 2020. ISSN 2206-5865. doi: 10.1071/ES19035.



Figure 5. Zonally averaged trend in apparent oxygen utilisation ($\frac{d\text{AOU}}{dt}$, first column) and the contribution from trends in ideal-age ($S_{\Delta\text{age}}^{\text{AOU}} \times \frac{d\text{age}}{dt}$, second column) under the SSP5-8.5 climate change scenario simulated with five Earth system models: MPI-ESM1.2-LR, ACCESS-ESM1.5, IPSL-CM6A-LR, MIROC-ES2L, NorESM2-LM. The remainder ($B + \varepsilon$, third column) is computed as the difference between the two aforementioned components (see Eq. 3). Trends are computed for the period from 2015 to 2099 and are zonally averaged on the four water-masses considered in this study, accounting only for grid points with significant trends (p-value > 0.05).